

# Optical pumping: Exciting optical and RF transitions in a double-resonance setup to perform spectroscopy on the hyperfine sublevels of the ground state of Rubidium

Max N. Frankel\*

*Department of Physics and Astronomy,  
Stony Brook University*

(Dated: March 20, 2023)

## **Abstract:**

While this senior laboratory experiment is really about the spectroscopy of hyperfine sublevels, optical pumping plays a vital role, and thus the title “Optical Pumping” is appropriate. The history of optical pumping in a double-resonance setup is deeply intertwined with the early developments of quantum mechanics and its description of atoms, and the concepts learned when conducting this experiment are still applicable in a wide range of atomic physics experiments today. In this report, we first discuss the history and theory behind optical pumping, and then go on to show how our optical pumping setup can be used to observe various energy level splittings that emerge from the non-classical treatment of the electron in the potential of an alkali atom. We use our measurements of these splittings to calculate the earth’s local magnetic field, Landé g-factors for the two most common isotopes of rubidium, and verify the Breit-Rabi formula.

## **I. INTRODUCTION**

### **A. Developing an understanding of atomic structure in the early 20th century: The Zeeman effect and Landé g-factor**

The pace at which atomic physics progressed in the early 20th century is remarkable. The existence of subatomic particles, namely electrons, wasn’t discovered until Thomson’s experiments with cathode rays in 1897 [1]. This discovery opened the floodgates for atomic physics research, and many new discoveries came rushing out to follow.

One such discovery was that of Pieter Zeeman, a Dutch physicist who had been investigating the connections between magnetism and light. Just a year earlier, armed with the newly developed technology of the diffraction grating, Zeeman had found that the spectral lines of a sodium flame became broadened and split in the presence of an external magnetic field. With the discovery of the electron, Zeeman was able to explain this splitting and broadening classically, by considering oscillating electrons as the source of emitted radiation in the sodium flame, and that their oscillation would be altered in an external magnetic field [2].

Then confusion came in an experimental discovery by Friedrich Paschen and Ernst Back in 1913 of two types of Zeeman splitting: one that they dubbed “normal” and one “anomalous” [3]. The normal Zeeman effect occurs when dealing with atomic states that have a net spin of 0 (singlet), while the anomalous Zeeman effect occurs when dealing with non-zero spin states. The problem was that, back in 1913, there was no concept of electron spin. In fact, electron spin was proposed in 1925 as a direct result of work done to understand the anomalous Zeeman effect [4]. Technically, Ralph Kronig came up

with the idea of electron spin first, as a 20-year old on a visit to Landé in 1925, but his findings were dismissed when he shared them with Wolfgang Pauli [5]. Uhlenbeck and independently came to the same conclusion later that year and published their results, and are more commonly credited with the discovery.

On the way to discovering spin, attempting to derive the Zeeman effect drove the physicists Sommerfeld and Debye to introduce the concept of space quantization to Bohr’s atomic model in 1916 [6], stating that the projection of the electron’s orbital angular momentum vector along the direction of an external magnetic field was quantized, and describing this quantization with the quantum number  $m$ .

In 1921, the physicist Alfred Landé created a model for the Zeeman effect, based off of empirical results [7]. The quantization of angular momenta was now understood, but his model split off from the accepted theory by allowing for the existence of electronic states with half-integer multiples of angular momentum quanta, in order to explain the existence of doublets while still maintaining the  $\Delta m = \pm 1, 0$  selection rule. His work involved the assumption that angular momentum quanta are vectors and that atomic angular momenta are combined by vector addition that is also subject to quantization. Although initially looked down upon by other physicists for its lack of theoretical justification, Landé’s g-factor and vector model turned out to be an important step towards discovering electron spin, interpreting the results of the Stern-Gerlach experiment, and formulating the Pauli exclusion principle [3][6].

### **B. Optical pumping and Alfred Kastler**

Alfred Kastler’s journey with optical pumping is well-outlined in his Nobel lecture and a 1967 article in *Science* [8][9].

The story begins with a young physicist in the 1920s, setting out into the nascent field of quantum mechanics.

---

\* max.frankel@stonybrook.edu

Kastler wrote that he became particularly interested in the conservation of angular momentum in the scattering of light from atoms after reading Arnold Sommerfeld's *Atombau und Spektrallinien* [10] in his studies at the Ecole Normale Supérieure. A Polish physicist working under Sommerfeld, Wojciech Rubinowicz, had, in 1918, shown that the application of conservation of angular momentum led to selection rules for atomic transitions regarding the azimuthal quantum number, corresponding to the polarization of light. These selection rules play a key role in the concept of optical pumping.

Kastler himself became involved in scattering experiments that studied the polarization of scattered light. Excitement came in 1931, when Indian Physicists Raman and Bhagavantam realized that these types of scattering experiments were evidence of the existence of photon spin [11]. Indian physicist Satyendranath Bose had already predicted the quantization of photon polarization into two states in a 1924 paper where he re-derived Planck's formula for blackbody radiation purely from statistical mechanics and the assumption of quantization, as he found Einstein's derivation to have "insufficient logical foundation." In that paper, Bose had found that an additional factor of 2 was needed to arrive at the proper number of cells in the phase space volume, and Raman and Bhagavantam claimed that Bose had guessed that this came from an intrinsic spin of the photon [12].

While at the Ecole Normale Supérieure, for his thesis in 1936, Kastler realized that circularly polarized light could be used to polarize an atomic vapor in successive transitions and selectively excite different magnetic sublevels of the Mercury atom [13]. Years later, this thesis work became very important when Kastler and a former student, Jean Brossel, devised an experiment to measure magnetic resonances between Zeeman sublevels of excited states. Brossel had been working under Francis Bitter at MIT, an American physicist who had been attempting to detect radio-frequency (RF) resonances optically [14], following the work of Rabi [15], Lamb, and Retherford [16] in developing nuclear magnetic resonance in the mid-1940s. Bitter saw the potential for the detection of RF resonances in weak magnetic fields to be used to measure Landé  $g$ -factors, gain information about nuclear spins, and search for additional hyperfine structure. His method involved studying the polarization of the edges of spectral lines. However, Kastler noted, Bitter's experiments did not work.

Kastler and Brossel's experiment for detecting RF resonances involved an optical resonance and an RF oscillating magnetic field, exactly as we do in this optical pumping experiment at Stony Brook today. Following his own thesis work, Kastler "pumped" a vapor of mercury atoms with circularly polarized light to form a concentration either in the positive or negative magnetic sublevels of the ground state, thus polarizing the vapor and creating a non-Boltzmann distribution. By applying an external magnetic field, Kastler knew that the ground state Zeeman sublevels would split apart. He realized

that one could then detect RF transitions between the Zeeman sublevels by varying the frequency of an RF oscillating magnetic field and observing the intensity of the light passing through atoms at an optical resonance [17].

Together with Jean Brossel, Kastler went on to explore many questions within optical pumping, such as the relaxation times of atomic vapors from non-Boltzmann distributions, the effects of buffer gases, measurements of the Landé factors, and multi-photon transitions. In 1966, Alfred Kastler was awarded the Nobel Prize "for the discovery and development of optical methods for studying Hertzian resonances in atoms."

### C. The importance of optical pumping

Optical pumping has broad applications, and its concept has remained relevant over the past century. Its application has ranged from creating the population inversion necessary for the first laser back in the 1960s [18], to making the first measurements of light-shift necessary for laser cooling and driving concepts such as Sisyphus cooling and Raman cooling in the 70s, 80s, and 90s [19], to orienting spins in spintronics in the past 20 years [20].

As stated by Cohen-Tannoudji in his 1998 Nobel prize lecture: "optical pumping is one of the first examples of manipulation of atoms by light" [19]. Since then, light has become one of the main tools for an atomic physicist, especially when working with neutral atoms.

## II. THEORY

### A. The nonrelativistic atomic model and its energy levels

Rb is an alkali atom with a single valence electron. The closed shells form a spherically symmetric core that shields the nuclear charge. Outside of this core, the electrical potential is approximately identical to that of the hydrogen atom. Because the valence electron orbital radius is much larger than the radius of this core, the analytic solutions to the hydrogen wavefunction can be used to approximate Rb's valence electron wavefunctions, which have no analytic solution [21]. In order to improve our approximation, we can calculate numerous corrections as perturbations, using perturbation theory.

The hydrogen wavefunctions are the solutions to the Schrödinger wave equation of an electron in the Coulomb potential of a proton [22].

$$i\hbar \frac{\partial}{\partial t} \psi = \hat{H} \psi = \left( \frac{\hbar^2}{2m_e} \nabla^2 - \frac{1}{4\pi\epsilon_0} \frac{e^2}{r} \right) \psi$$

The Hamiltonian for an alkali atom differs in that the nuclear charge is  $Ze$  (for some integer  $Z$  equal to the

number of protons) instead of  $e$ , there are multiple electrons, and there is an additional term representing the interaction between the electrons. When considering the valence electron outside of the spherical core of electrons, we assume that the interaction between electrons counteracts the greater nuclear charge of the alkali atom, yielding the same Hamiltonian as hydrogen.

$$\hat{H} = \sum_i \left( \frac{\hbar^2}{2m_e} \nabla_i^2 - \frac{1}{4\pi\epsilon_0} \frac{Ze^2}{r_i} \right) + \sum_{i,j} \frac{1}{4\pi\epsilon_0} \frac{e^2}{|r_i - r_j|} \quad (1)$$

The hydrogen wavefunctions consist of radial solutions that depend on the quantum number  $n$  multiplied by spherical harmonics that depend on quantum numbers  $l, m$ .

$$\psi_{n,L,M} = R_n(r)Y_{L,M}(\theta, \phi)$$

The quantum state of the hydrogen wavefunction can be determined by applying a set of commutative operators describing measurements,  $\hat{H}$ ,  $\hat{L}^2$ , and  $\hat{L}_z$ . When acting on a quantum state  $\psi_{n,L,M}$ , they return eigenvalues  $E_n, L, M$ :

$$\begin{aligned} \hat{H}\psi_{n,L,M} &= E_n\psi_{n,L,M} \\ \hat{L}^2\psi_{n,L,M} &= L(L+1)\psi_{n,L,M} \\ \hat{L}_z\psi_{n,L,M} &= M\psi_{n,L,M} \end{aligned}$$

where

$$E_n = -\frac{m_e}{2\hbar^2} \left( \frac{e^2}{4\pi\epsilon_0} \right)^2 \frac{1}{n^2}$$

In this non-relativistic model, the energy levels are determined solely by  $n$ , and the different  $L, M$  form degenerate sublevels for a given  $n$ .

In this report, we are working with Rubidium. Following the aufbau principle, the core electrons of Rb fill up the orbitals  $n = 1, 2, 3, 4$ , meaning that, in the ground state, the valence electron is in  $n = 5$ .

## B. Correction to energy levels due the quantum defect

The potential experienced by the Rb valence electron is only identical to that of Hydrogen's electron outside the spherical shell of electrons. Inside this shell, the nuclear charge is no longer shielded, and the potential changes with  $Ze/r^2$  instead of  $e/r^2$ . The valence electron experiences a shift in energy depending on how much its wavefunction overlaps with the the core, leading to a shift in energy that is dependent on  $L$ . This energy shift is referred to as the quantum defect [21].

For rubidium, the quantum defect causes the normally degenerate 5S and 5P levels to become separated by an energy on the order of 1.6eV [23].

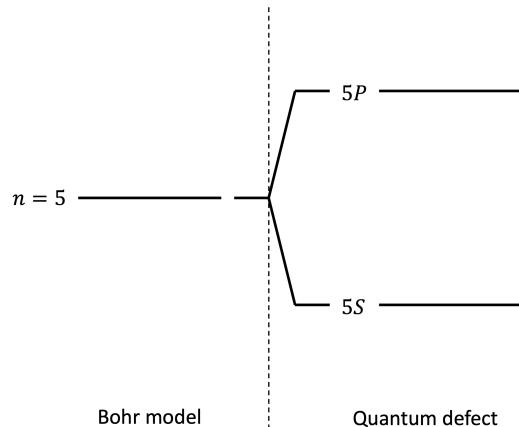


Figure 1. Diagram showing how the quantum defect lifts the degeneracy of the  $S$  and  $P$  sublevels within the  $n = 5$  energy level of the Bohr model. The  $L = 2, 3, 4, \dots$  sublevels receive an energy shift as well, but are considered in this experiment and so are not pictured.

## C. Relativistic corrections to the hydrogen model energy levels

The Hamiltonian of Eq. 1 is non-relativistic. Thus, the relativistic Hamiltonian for an atom, given by the Dirac formula, gives a better model for our Rb atom [24]. Relativistic treatment of the electron leads to additional terms in the Hamiltonian of Eq. 1, referred to as relativistic corrections.

The purpose of this lab was not to explore all of the different corrections. The corrections of interest were those which lift some degeneracy between quantum states, splitting energy levels, as this creates extra transitions in the absorption spectrum that can be easily observed.

The three relativistic corrections that cause observable splitting are spin-orbit coupling, hyperfine splitting, and the Zeeman effect, all of which deal with the potential energy of a magnetic moment  $\vec{\mu}$  in a magnetic field  $\vec{B}$ .

$$E = -\vec{\mu} \cdot \vec{B}$$

### 1. Splitting of energy levels due to spin-orbit coupling

In Rb, spin-orbit coupling creates splitting of the 5P energy level of around 0.03eV, two orders of magnitude smaller than the splitting between the 5S and 5P levels [23].

In the reference frame of an electron, the orbital motion of the nucleus creates a magnetic field. This magnetic field interacts with the electron's intrinsic magnetic

moment,  $\mu_e$ . The Hamiltonian for magnetic moment in an external magnetic field is given by [21]

$$\hat{H}_{SO} = -\vec{\mu}_e \cdot \vec{B} \quad (2)$$

Now, for the orbiting electron,  $\vec{B} \propto \vec{L}$ , the electron's orbital angular momentum, and  $\vec{\mu}_e \propto \vec{S}$ , the electron's spin [23]. Therefore,

$$\hat{H}_{SO} \propto \hat{L} \cdot \hat{S}$$

The Hamiltonian composed of both  $\hat{H}_0$  and  $\hat{H}_{SO}$  has a term proportional to  $\hat{L} \cdot \hat{S}$ , and thus  $\hat{L}_z$  no longer commutes with the Hamiltonian. Thus a new basis is required to describe the state  $\psi$ .

$\hat{J} = \hat{L} + \hat{S}$  does commute with the Hamiltonian, and thus  $\hat{L}^2$ ,  $\hat{S}^2$ , and  $\hat{J}^2$  become the new set of operators used to describe a state  $\psi$ .

For an electron,  $S = 1/2$ , and  $L = 0, 1, 2, \dots$ . For the  $5S$  energy level of Rb,  $L = 0$  and so there is no splitting, as  $J = S$ . However, for the  $5P$  energy level of Rb,  $L = 1$ , and thus  $J = L \pm S$  can take on the values  $J = 1/2, 3/2$ . These two states have different energy, as seen in Eq. 2, and thus the  $5P$  energy level is split.

A common notation to keep track of  $L, S$ , and their relative orientation is shown below:

$$^{2S+1}L_J$$

Using this notation, we can say that  $5P$  splits into  $^2P_{1/2}$  and  $^2P_{3/2}$ .

Because  $L = 0$  for  $5S$ ,  $J$  is simply equal to  $S$ , and thus is written as  $^2S_{1/2}$ .

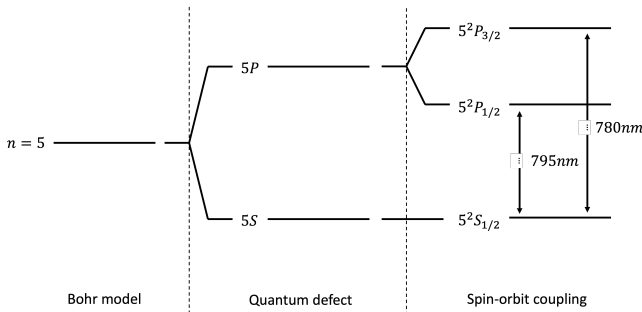


Figure 2. Diagram showing how spin-orbit coupling splits the  $5^2P$  energy level of Rb into  $^2P_{1/2}$  and  $^2P_{3/2}$  levels. While the splitting between the S and P levels is on the order of 1eV, the splitting between  $^2P_{1/2}$  and  $^2P_{3/2}$  due to spin orbit coupling is on the order of  $10^{-2}eV$ .

Only the  $5S_{1/2}$  and  $5P_{1/2}$  levels are of interest for this report.

## 2. Hyperfine structure

The hyperfine splitting of each energy level occurs on a scale another few orders of magnitude smaller than the spin-orbit coupling. Rb has a nuclear magnetic moment  $\vec{\mu}_I$ , which interacts with the total magnetic field created by the electron  $\vec{B}_e$ .

$$\hat{H}_{HF} = -\vec{\mu}_I \cdot \vec{B}_e$$

The nucleus's magnetic moment is proportional to the nuclear spin  $\hat{I}$ , and the magnetic field of the electron  $\vec{B}_e$  is created from the sum of the magnetic moments of the electron's intrinsic magnetic moment, proportional to the sum of its spin  $\hat{S}$  and the magnetic moment arising from its orbital motion, proportional to  $\vec{L}$ . Thus,  $B_e \propto \hat{L} + \hat{S} = \hat{J}$ , and therefore,

$$\hat{H}_{HF} \propto \hat{I} \cdot \hat{J}$$

Again, we must choose a new set of operators. In this case, a new operator  $\hat{F} = \hat{I} + \hat{J}$  is defined, and the operators  $\hat{F}^2$ ,  $\hat{I}^2$ ,  $\hat{J}^2$ , and  $\hat{F}_z$  and their eigenvalues are used to describe the atom's state  $\psi$ .

$$\hat{F}^2\psi = F(F+1)\psi$$

$$\hat{I}^2\psi = I(I+1)\psi$$

$$\hat{J}^2\psi = J(J+1)\psi$$

$$\hat{F}_z\psi = M_F\psi$$

where

$$M_F = -F, -F+1, \dots, F-1, F$$

Thus, each energy level determined by the corrections thus far can take on two values  $F = I \pm J$ . For each level corresponding to some  $F$ , there are  $2F+1$  sublevels corresponding to the different possible orientations of  $\vec{F}$  with the chosen quantization axis.

The values of  $I$  for  $^{85}\text{Rb}$  and  $^{87}\text{Rb}$  are shown in the table below:

$I$ for $^{85}\text{Rb}$	$I$ for $^{87}\text{Rb}$
$5/2$	$3/2$

Table I. This table represents the nuclear spin value for each respective isotope of Rb

So far, the corrections to both  $^{85}\text{Rb}$  and  $^{87}\text{Rb}$  have been equal. Hyperfine splitting is a correction that differs between the two isotopes.

For both the  $5S_{1/2}$  and  $5P_{1/2}$  levels of  $^{85}\text{Rb}$ , the energy levels are split into two values, corresponding to the two values of  $F = 5/2 \pm 1/2 = 2, 3$ .

For both the  $5S_{1/2}$  and  $5P_{1/2}$  levels of  $^{87}\text{Rb}$ , the energy levels are split into two values, corresponding to the two values of  $F = 3/2 \pm 1/2 = 1, 2$ .

A diagram of the full set of corrections accounted for in this report for both  $^{85}\text{Rb}$  and  $^{87}\text{Rb}$  is shown in Fig 3

### 3. Zeeman splitting

If we now apply an external magnetic field along the chosen quantization axis  $\hat{z}$ , there will be additional potential energy from the net dipole moment of the Rb atom interacting with the external field.

$$\hat{H}_{Zeeman} = -\mu_{atom} \cdot B_{ext}$$

However, we can only treat this energy as a perturbation if it is small compared to our Hamiltonian. When the perturbation is much smaller than that which creates hyperfine splitting,

$$\hat{H}_{Zeeman} = g_F \frac{\mu_B B_{ext}}{\hbar} \hat{F}_z$$

where [25] [26]

$$g_F = g_J \frac{F(F+1) - I(I+1) + J(J+1)}{2F(F+1)} + g_I \frac{F(F+1) + I(I+1) - J(J+1)}{2F(F+1)} \quad (3)$$

and  $g_F$  is known as the Landé g factor.

By first order perturbation theory, this causes an energy shift that affects each magnetic sublevel  $M_F$  differently:

$$\Delta E_{|F, M_F\rangle} = \mu_B g_F M_F B_z \quad (4)$$

This splitting of the  $M_F$  sublevels is known as the Zeeman effect. Note that this means that the energy difference between adjacent  $M_F$  sublevels is  $\mu_B g_F B_z$ . These energy differences are what we can actually measure experimentally. By varying  $B_z$  and measuring the energy differences, one can calculate  $g_F$  and the earth's magnetic field at the site of the experiment.

Eq. 4 is a good approximation for small magnetic fields. There is, in fact, an analytic solution to the energy shifts of the  $5^2P_{1/2}$  ground state manifold of Rb, given by the Breit-Rabi formula:

$$E_{|J=1/2, m_J, m_I\rangle} = -\frac{\Delta E_{hfs}}{2(2I+1)} + g_I \mu_B m B \pm \frac{\Delta E_{hfs}}{2} \left( 1 + \frac{4mx}{2I+1} + x^2 \right)^{1/2} \quad (5)$$

where  $m = m_I \pm m_J = m_F$ ,

$$x = \frac{(g_J - g_I) \mu_B B}{\Delta E_{hfs}}$$

This formula and the values of  $E_{hfs}$ ,  $g_I$ ,  $g_J$  can be found in Steck's Alkali data [25].

For  $m = M_F = -F$ , the Breit-Rabi formula can be written as

$$E_{|J=1/2, m_J, m_I\rangle} = \Delta E_{hfs} \frac{I}{2I+1} - \frac{1}{2}(g_J + 2I g_I) \mu_B B$$

The calculated energy shift according to the Breit-Rabi formula was calculated for  $F = 3$  in Rb85 and  $F = 2$  in Rb87, and is shown in Fig. 4 below:

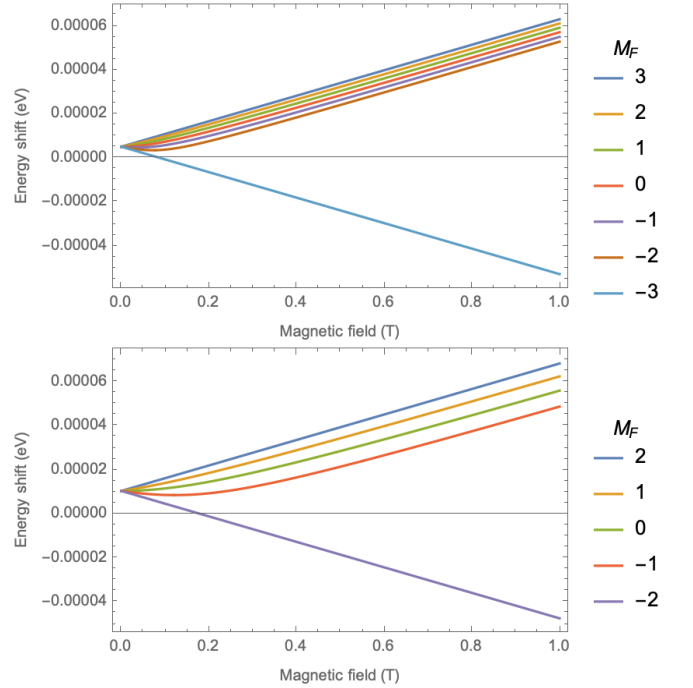


Figure 4. Calculated energy shift for Rb85 (top) and Rb87 (bottom) according to the Breit-Rabi formula (Eq. 5)

However, in this experiment, the maximum magnetic field achievable was about  $0.8\text{mT}$ . Let's focus in on this region in our graphs.

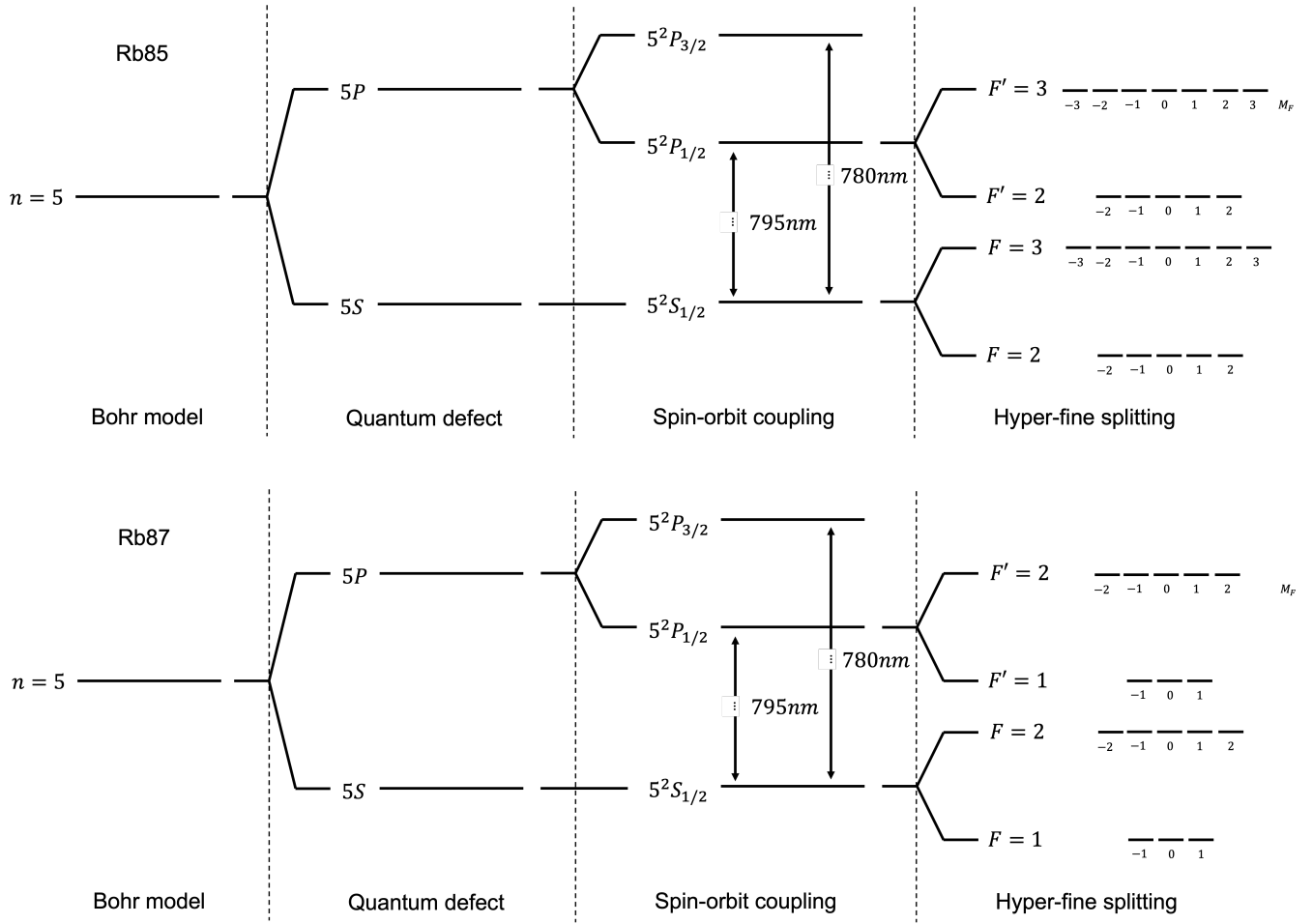
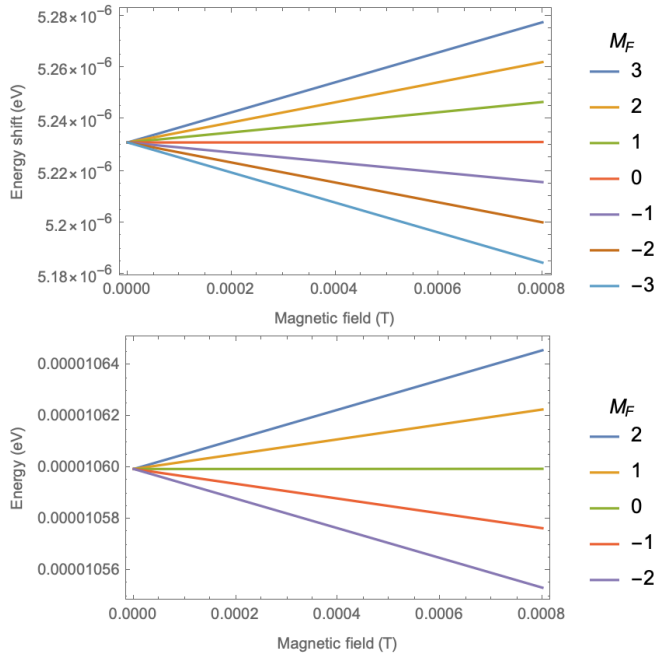


Figure 3. Diagrams showing the energy corrections to  $^{85}\text{Rb}$  and  $^{87}\text{Rb}$  due to multiple electrons, spin-orbit coupling, and hyper-fine splitting in order of largest to smallest in magnitude. The two isotopes differ only after the consideration of hyper-fine splitting, where their different nuclear magnetic moments  $I$  lead to different possible values for  $F = I \pm J$ .



As seen in Fig. 5, the energy difference between adjacent  $M_F$  sublevels at our achievable field strengths is very close to equal as magnetic field increases, showing that Eq. 4 is a good approximation.

With spectroscopy, the energy levels themselves can't be measured, but transitions between them can. Transition frequencies (energy/h) between adjacent  $M_F$  sublevels were calculated and are shown in Fig. 7.

Figure 5. The graphs from Fig. 4, but over the range of magnetic fields achievable in the experimental setup. Top is  $^{85}\text{Rb}$  and bottom is  $^{87}\text{Rb}$ .

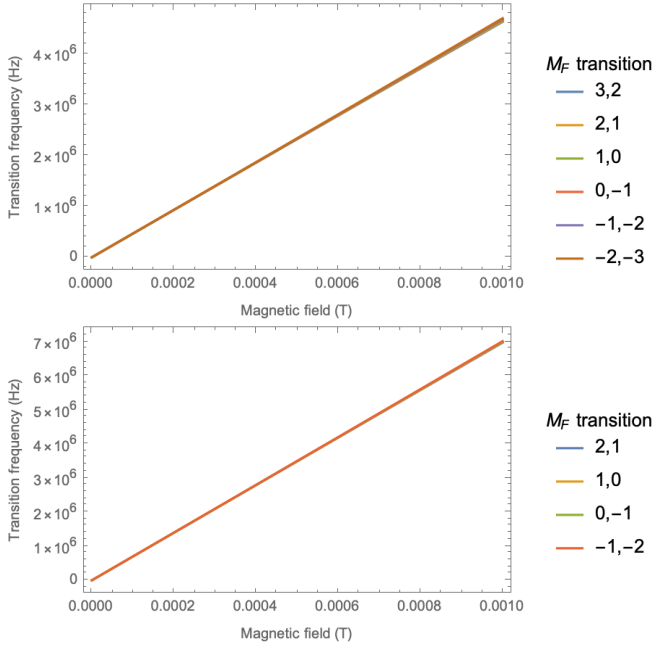


Figure 6. Theoretical calculation of frequency needed to excite transitions between adjacent  $M_F$  sublevels over magnetic field for Rb85 (top) and Rb87 (bottom). There appears to be only one line because the frequencies are very close together.

The transitions are very close in energy, but not equal. The slight difference is only clear when plotting the difference between adjacent transitions.

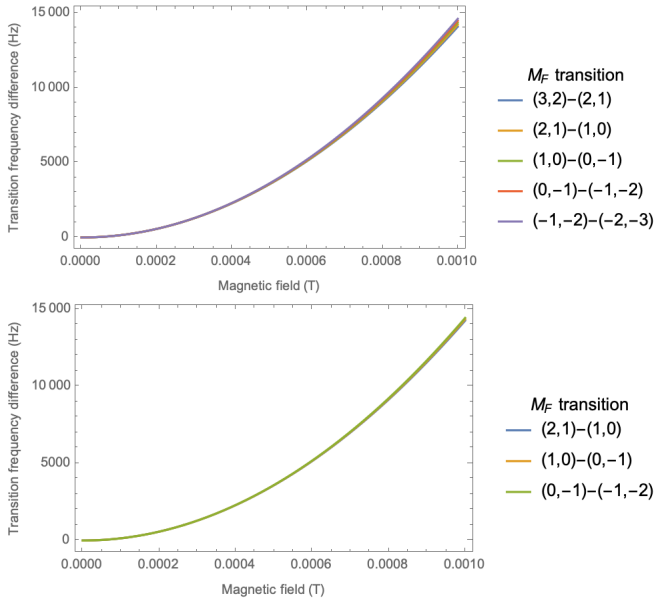


Figure 7. Theoretical calculation of difference in transition frequencies over magnetic field for Rb85 (top) and Rb87 (bottom). While the transitions are relatively close in frequency, all increasing linearly by about  $10\text{ MHz}$  per  $\text{mT}$  as shown in Fig. 7, this graph shows how the transitions split apart, on the order of  $10\text{ kHz}$  away from their nearest neighbor as the magnetic field increases to  $1\text{ mT}$

In this lab, we measured the RF resonances between adjacent  $M_F$  sublevels as a function of magnetic field, and compared to theoretical values.

#### D. Using light to determine differences between atomic energy levels

An atom can transition between two energy levels when stimulated by a photon with energy very close to the difference between two energy levels. For a photon,

$$E_{\text{photon}} = h\nu$$

where  $h$  is the Planck constant and  $\nu$  is the photon frequency. The condition when  $\nu$  is such that  $E_{\text{photon}}$  is exactly equal to the energy difference between two levels is called resonance. Atoms can absorb light that is not perfectly resonant with a transition, but the probability of absorption increases the closer the frequency of light is to resonance.

The allowed transitions are determined by the selection rules. For an unpolarized photon, only transitions for which  $\Delta M_F = -1, 0, 1$  are allowed. A right-hand circularly polarized photon, denoted as  $\sigma_+$ , causes transitions for which  $\Delta M_F = +1$ . For a left-hand circularly polarized  $\sigma_-$  photon,  $\Delta M_F = -1$  [27].

By scanning the frequency  $\nu$  of light illuminating a gas of atoms, the location of resonances corresponding to different transitions can be observed as dips in the amount of light transmitted through the gas. The rate at which photons are absorbed by a gas of atoms with respect to their detuning  $\nu - \nu_0$  from an atomic resonance  $\nu_0$  follows the Voigt profile [27],

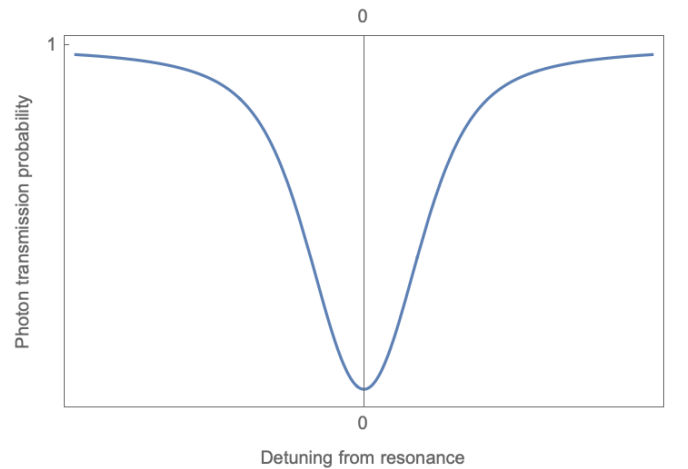


Figure 8. The Voigt profile models the absorption probability of a photon detuned from an atomic resonance. Even though atoms have discrete energy levels, photons do not need to be perfectly resonant with a transition in order to cause stimulated absorption and emission

where the center of the dip corresponds to resonance with the atomic transition.

### E. Optical pumping

Consider the  $5^2S_{1/2}$  and  $5^2P_{1/2}$  energy levels in  $^{87}\text{Rb}$ . For a gas of  $^{87}\text{Rb}$  in thermal equilibrium, each energy state will be populated by some fraction of the total number of atoms, following the Boltzmann distribution. In fact, the spacing between hyperfine levels is so small that the thermal energy of a vapor of Rb becomes comparable to the spacing at about  $300\text{mK}$ . We are operating at room temperature - around  $300\text{K}$ . Thus, even in the presence of an external magnetic field, the populations among the different hyperfine levels is approximately equally distributed in thermal equilibrium.

Suppose  $795\text{nm}$  light is shone onto the gas, and that the light has a linewidth great enough that it allows for transitions between any of the sublevels within the  $5^2S_{1/2}$  level to and from any sublevels within the  $5^2P_{1/2}$  level, but not great enough to create transitions up to any of the sublevels within  $5^2P_{3/2}$ .

There are selection rules for allowed transitions due to stimulated absorption that depend on the polarization of light. For right-hand circularly polarized light along the  $\hat{z}$  direction, denoted  $\sigma_+$ , the selection rule requires that  $\Delta M_F = +1$ . The allowed transitions are illustrated in Fig. 9.

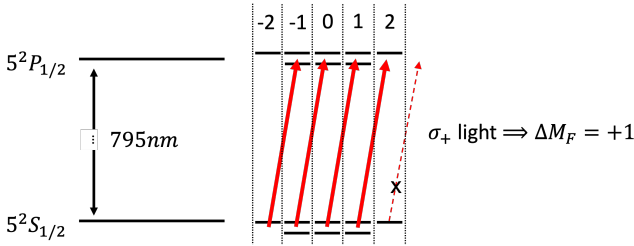


Figure 9. Diagram of the allowed  $\Delta M_F = +1$  transitions from  $5^2S_{1/2}$  to  $5^2P_{1/2}$  states of  $^{87}\text{Rb}$  by stimulated absorption of  $\sigma_+$  light at  $795\text{nm}$ . Clearly, all of the  $5^2S_{1/2}$  states can absorb the  $\sigma_+$  light except for  $F = 2, M_F = 2$ . A similar diagram can be drawn for  $\text{Rb}85$ .

Clearly, if a gas of  $^{87}\text{Rb}$  atoms is illuminated with  $\sigma_+$  light at  $795\text{nm}$ , atoms in the  $F = 2, M_F = 2$  state cannot undergo stimulated absorption.

Once in an  $5^2P_{1/2}$  excited state, atoms can transition back down to the ground  $5^2S_{1/2}$  states through spontaneous emission. Because spontaneous emission does not have a set polarization, the selection rule requires that  $\Delta M_F = +1, 0, -1$  in any transition by spontaneous decay. Only spontaneous decay from  $5^2P_{1/2}$  to  $5^2S_{1/2}$  is considered, as the transition frequency of spontaneous decay and corresponding lifetime of the  $5^2S_{1/2}, F = 2$  state is much smaller than that of any of the  $5^2P_{1/2}$  states. An example of the allowed transitions due to

spontaneous decay from the  $F' = 1, M_F = 1$  is shown in Fig. 10.

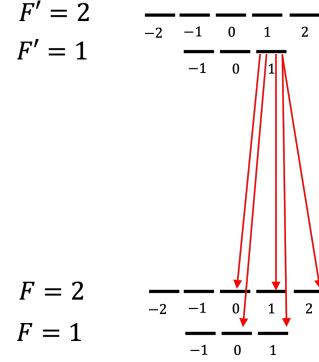


Figure 10. Diagram of the allowed transitions due to spontaneous emission from the  $F' = 1, M_F = 1$  state. Spontaneous emission from any of the  $5^2P_{1/2}$  can have  $\Delta M_F = 1, 0, -1$ .

Once the atom decays back down to a  $5^2S_{1/2}$  state, it can absorb  $\sigma_+$  light again and undergo a  $\Delta M_F = +1$  transition again. Combined with the fact that the probabilities of  $\Delta M_F = +1, 0, -1$  are equally likely in spontaneous emission, in the presence of  $\sigma_+$  light, atoms are “pumped” towards the maximum  $M_F$  values.

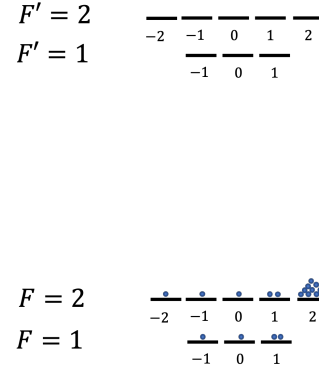


Figure 11. For many atoms and after many cycles of absorption and emission, there will be a buildup of atoms in the ground state with maximum  $M_F$ .

Note that the selection rules make it so that, once an atom is in the  $F = 2, M_F = 2$  state, it is stuck there, and cannot decay or absorb light. Thus,  $F = 2, M_F = 2$  is referred to as a metastable state. Of course, processes such as collisions between atoms and spontaneous emission down to  $F = 1, M_F = 1$  do allow atoms in  $F = 2, M_F = 2$  to transition out of the metastable state, but if the characteristic times of these processes is much longer than the characteristic time of stimulated absorption of the  $\sigma_+$  light, a large fraction of the population is pumped away from thermal equilibrium and into the  $F = 2, M_F = 2$  state.



## F. Absorptive cross section and Beer's Law

The attenuation of light as it passes through an absorptive medium composed of identical two-level systems is described by Beer's law [27] (page 115)

$$I(z, T) = I(0) \exp(-a(T)z) \quad (6)$$

where  $I$  is the intensity of light,  $T$  is temperature,  $z$  is the propagation distance travelled through the medium, and  $a(T)$  is the absorption coefficient as a function of temperature  $T$ , defined to be

$$a(T) \approx \sigma \frac{g_2}{g_1} n(T) \quad (7)$$

where  $\sigma$  is the absorption cross section,  $g_1$  and  $g_2$  are the degeneracies of the lower and higher energy states involved in the transition, respectively, and  $n(T)$  is the density of atoms as a function of temperature. Therefore, in the experimental setup, the attenuation through the Rb cell of length  $z_{cell}$  as a function of temperature is

$$I(T) = I(0) \exp(-\sigma n(T)z_{cell}) \quad (8)$$

Taking the logarithm of both sides of Eq. 8,

$$\log I(T) = \log I(0) - \sigma n(T)z_{cell} \quad (9)$$

As seen in Eq. 9,  $\log I(T)$  vs  $n(T)z_{cell}$  is a linear relationship with slope  $-\sigma$ .

The theoretical value of the absorption cross section is [21]

$$\sigma = 3\lambda^2/2\pi \quad (10)$$

## III. EXPERIMENTAL SETUP

### A. Experimental techniques

#### 1. Measurement of Zeeman shift at low external magnetic field for Rb87

The primary goal of this experiment was to measure the Zeeman shift as a function of external magnetic field. Suppose that a vapor of Rb87 is continuously illuminated with 795nm  $\sigma_+$  light, causing atoms to become optically pumped to the  $F = 2, M_F = 2$  state (for Rb85, it would be the  $F = 3, M_F = 3$  state), as shown in Fig. 11. Let's refer to the  $\sigma_+$  light as the pump light.

Now suppose that a small external field is applied along the  $\hat{z}$  direction so that Eq. 4 is a good approximation.

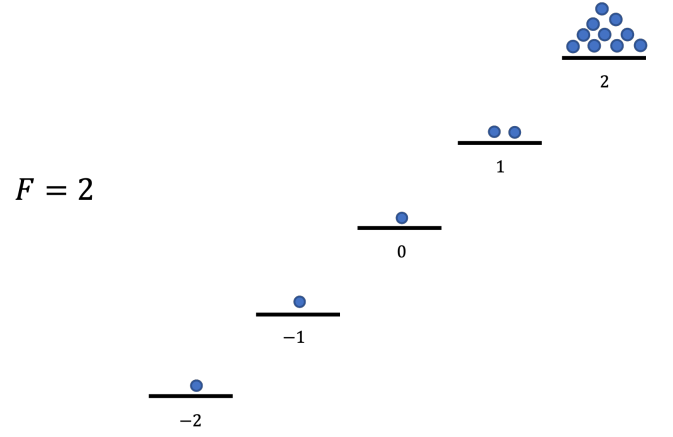


Figure 12. Zeeman splitting of the  $M_F$  sublevels of  $F = 2$  for Rb87

If additional electromagnetic radiation is shone in at resonance with the energy difference between the split  $M_F = 2$  and  $M_F = 1$  states for  $F = 2$ , atoms in the metastable  $F = 2, M_F = 2$  state can undergo stimulated emission and transition with  $\Delta M_F = -1$  to the  $M_F = 1$  state, in which they can absorb the pump light. If we observe the amount of pump light passing through the vapor, when the RF is on resonance, we will see a dip in the amount of pump light passing through, as it is being absorbed at a greater rate.

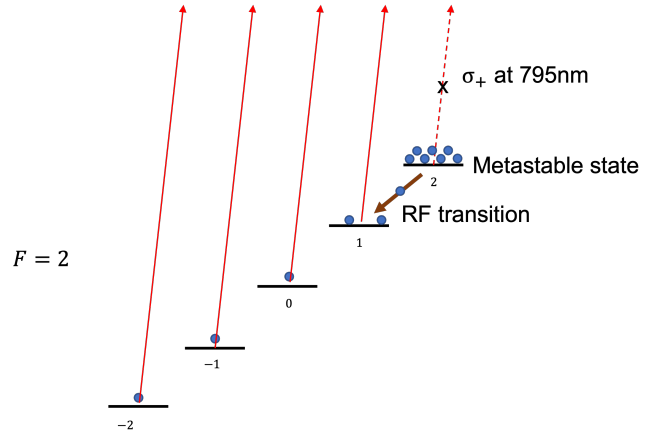


Figure 13. Atoms in the  $F = 2, M_F = 2$  state cannot absorb the 795nm  $\sigma_+$  light (red arrow) according to the selection rules. However, an RF photon can cause a transition to the  $F = 2, M_F = 1$  state (brown arrow), in which the atom can absorb the  $\sigma_+$  light

For the earth's magnetic field at Stony Brook of  $50\mu T$  [?] and  $\mu_B \approx 5 * 10^{-5} eV/T$ , Eq. 4 implies that the transition between  $M_F$  and  $M_F - 1$  states are on the order of  $2.5 * 10^{-11} eV$ , which corresponds to about  $600 kHz$

Thus, by applying radio frequency (RF) electromag-

netic radiation at varying frequency to the Rb vapor, the Zeeman shift was measured.

By creating an external magnetic field along the same direction as the earth's magnetic field, the Zeeman shift as a function of external magnetic field was measured.

## 2. Observation of non-linear Zeeman splitting at high external magnetic field

In practice, optical pumping does not pump every single Rb87 atom into the  $F = 2, M_F = 2$  state ( $F = 3, M_F = 3$  for Rb85). Collisions between atoms can cause state changes, and the rate of spontaneous emission from the  $F = 2, M_F = 2$  is low but does not 0. Thus, each  $M_F$  sublevel has some nonzero population. Due to pumping, the population increases with increasing  $M_F$ .

In low magnetic field, where the splitting between each  $M_F$  level is equal, an RF magnetic field resonant with the  $M_F = 2, 1$  transition is also resonant with the  $M_F = 1, 0$ , the  $M_F = 0, 1$ , and the  $M_F = -1, -2$  transitions. As the splitting between  $M_F$  levels differs in high magnetic field, there is a substantial difference in the resonant frequency of transitions between adjacent  $M_F$  sublevels, making them resolvable in spectroscopic measurement.

But why is there any visible change in transmission for transitions that do not involve the metastable state?

I assume that, due to the long state lifetime of the hyper-fine levels of  $5^2S_{1/2}$ , the continuous RF light causes Rabi oscillations. Averaged over time, these Rabi oscillations effectively equalize the populations in the two  $M_F$  states involved. Pumping is continually working against effects that bring the system back towards thermal equilibrium, and this Rabi oscillation means less pumping into the metastable state where atoms no longer absorb  $\sigma_+$  light. Less atoms in the metastable state means more atoms absorbing  $\sigma_+$  light, contributing to the dip in transmission of  $M_F$  light.

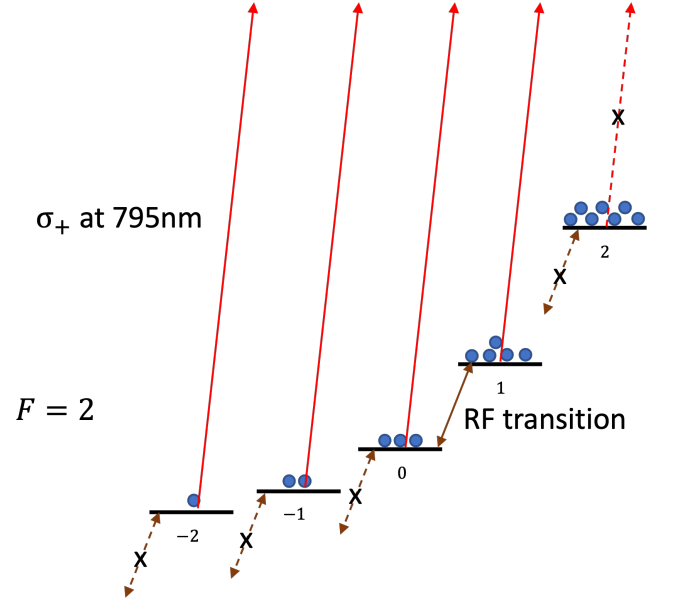


Figure 14. This diagram is for Rb87, with 795nm  $\sigma_+$  light in red and RF light in brown. The blue circles represent the population of atoms in each  $M_F$  state. In the Paschen-Back effect, the external magnetic field is strong enough that the transitions between adjacent  $M_F$  sublevels differ. Thus, a single  $\Delta M_F = 1$  transition can be isolated. In this case, the  $M_F = 1, 2$  transition is shown to be isolated, and atoms in the  $M_F = 0, 1$  states undergo Rabi oscillation between the two states, effectively equalizing their populations and thus working against optical pumping.

## B. Components

### 1. Rb cell and optics

Central to the experimental setup was the Rb cell, a glass cell containing both  $^{85}\text{Rb}$  and  $^{87}\text{Rb}$  isotopes. This glass cell was heated with a heat gun in order to increase the density of the Rb vapor inside the cell.

The 795nm light, corresponding to the transitions commonly referred to as the  $D_1$  line for Rb, was generated with a Rb lamp. A  $D_1$  filter was used to isolate the 795nm light produced by the lamp. A linear polarizer followed by a quarter waveplate was used to transform the polarization of the 795nm to  $\sigma_+$  with respect to the propagation direction,  $\hat{z}$ .

The light was focused into the Rb cell by a lens, and the light transmitted through the cell was focused onto a photodiode by another lens. The photodiode's output voltage was measured with an oscilloscope at 60dB gain. The use of 60dB gain was crucial in being able to resolve multiphoton transitions.

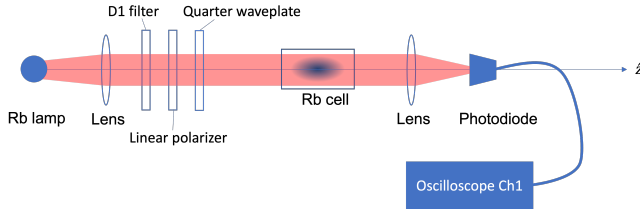


Figure 15. Optics involved in measuring the transmission of  $795\text{nm}$   $\sigma_+$  light through the Rb cell

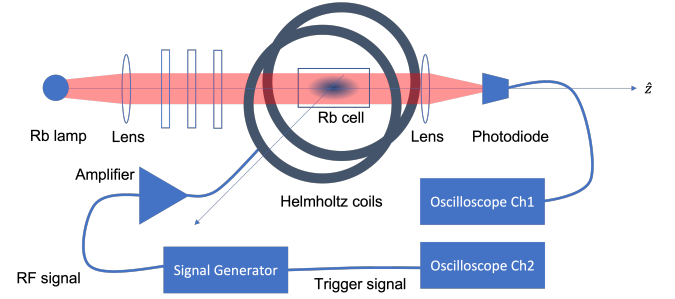


Figure 17. Diagram showing how the Helmholtz coils are used to create an oscillating magnetic field at RF within the Rb cell.

An example of the photodiode voltage and SG trigger recorded with the oscilloscope in a measurement are shown in Fig. 18:

## 2. Helmholtz coils for oscillating magnetic field

The oscillating RF magnetic field was created by a pair of Helmholtz coils oriented perpendicular to the  $\hat{z}$  direction. Thus, the RF photons were unpolarized, and could cause transitions where  $\Delta M_F = -1, 0, 1$ . Oscillating current was supplied to the coils by the amplified output of a signal generator (SG). The SG was set to sweep linearly through range of frequencies over time around some center frequency. The sweep time was set to  $1\text{s}$ , as certain features, such as multi-photon transitions, could not be resolved at lower sweep times. The SG output amplitude was adjusted with each measurement to ensure that the voltage was low enough not to overdrive the amplifier but high enough to observe a dip in absorption.

The SG output a square wave to Ch2 of the scope, which was used as a trigger for making measurements. The SG would sweep from its minimum to maximum value over the period of the trigger signal, with  $0\text{s}$  return time between each cycle.

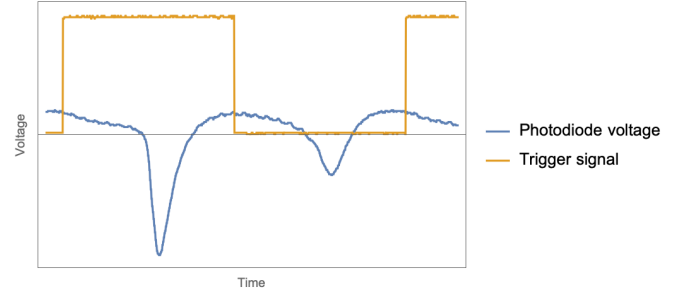


Figure 18. An example of the signals measured by channel 1 (blue) and channel 2 (yellow) of the oscilloscope for the setup in Fig. 17

In order locate the frequencies of the dips, the time axis was transformed to frequency by setting lowest frequency in the sweep at the first rising edge of the trigger signal and the highest frequency of the sweep at the second rising edge of the trigger signal. The voltage signals were normalized in the analysis of each measurement.

## 3. Maxwell coils for constant external magnetic field

In order to create an external magnetic field, three coils in the Maxwell arrangement surrounding the Rb cell were used. The Maxwell coils were oriented along the  $\hat{z}$  axis. Because the discussion of Zeeman splitting assumed the external field was along the  $\hat{z}$  direction, the whole apparatus was oriented such that  $\hat{z}$  pointed along the direction of the earth's magnetic field.

The Maxwell coils were supplied with current from a DC power supply. The current was measured with an ammeter in series.

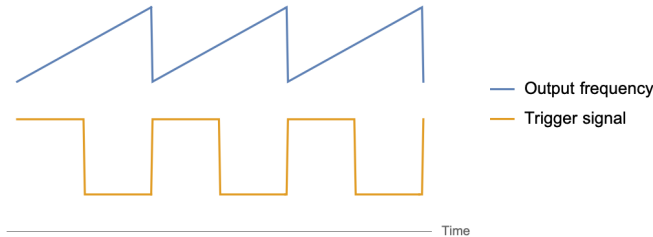


Figure 16. Diagram showing how the two outputs of the SG are related

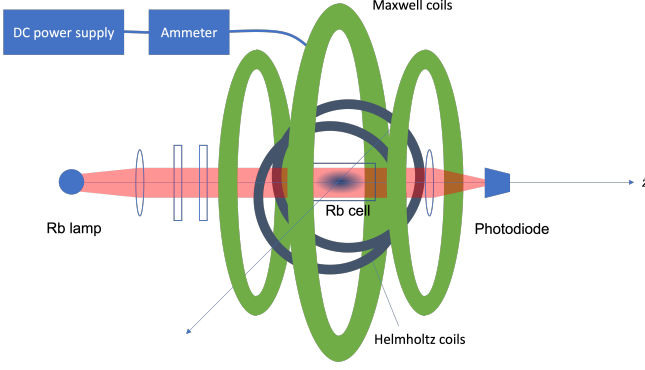


Figure 19. The Maxwell coils were oriented such that the magnetic field they created was aligned with the  $\hat{z}$  direction, parallel to the propagation direction of the  $\sigma_+$  light and the earth's local magnetic field.

The magnetic field of the Maxwell coils was calculated by approximating each coil as a current loop and applying the Biot Savart law [?]. The magnetic field of a current loop oriented along  $\hat{z}$  at a distance of  $z$ , a radius of  $R$ , and with  $N$  turns, as a function of current  $I$ , is

$$\vec{B}(I) = N \frac{\mu I}{2} \frac{R^2}{(R^2 + z^2)^{3/2}} \hat{z} \quad (11)$$

where  $\mu = 4\pi * 10^{-7} N/A^2$  is the permeability of free space.

The values of  $z$ , the diameter, and the number of turns for each of the coils are collected in Tab. II below:

Coil	$z$ location	Diameter	Number of turns
Large	$0 \pm 1cm$	$78.4 \pm 0.1cm$	$142 \pm 1$
Small	$\pm(26.5 \pm 0.1cm)$	$59.1 \pm 0.1cm$	$110 \pm 1$

Table II. Specifications of the Maxwell coils used to generate an external magnetic field

By summing together the magnetic fields produced by each coil according to Eq. 11, the magnetic field was calculated for a given current supplied by the DC power supply and measured with the ammeter shown in Fig 19.

Uncertainty in the calculated magnetic field for a single loop was estimated using the following equation:

$$\frac{\delta B}{B} = \sqrt{\left(\frac{\delta N}{N}\right)^2 + \left(\frac{\delta I}{I}\right)^2 + \left(\frac{\delta R}{R}\right)^2 + \left(3z \frac{\delta z}{z}\right)^2}$$

The uncertainty in the total magnetic field was estimated by adding the relative uncertainty of the magnetic field created by each loop in quadrature.

$$\frac{\delta B_{tot}}{B_{tot}} = \sqrt{\sum_{i=1}^3 \left(\frac{\delta B}{B}\right)^2}$$

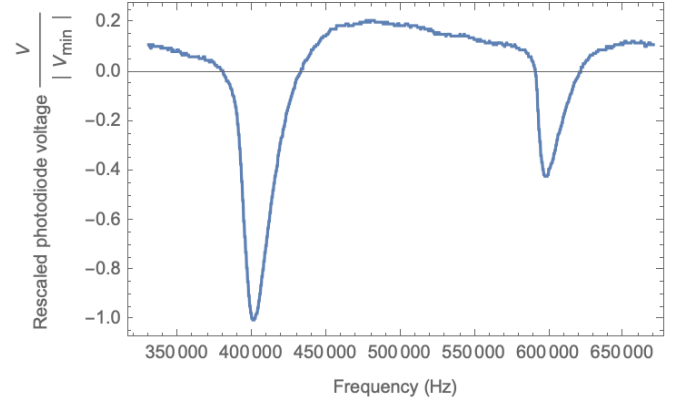


Figure 20. An example of how the time axis of the data shown in Fig. 18 was rescaled for locating transition frequencies

### C. Data analysis

Given a measurement such as that shown in Fig. 18, in order to find the transition frequencies corresponding to the centers of different absorption dips, the time axis of the scope was first transformed into frequencies. As shown in Fig. 16, at the first rising edge of the trigger signal, the SG output is at its lowest frequency, which is set by

$$f_{low} = f_{center} - f_{span}/2$$

where  $f_{center}$  and  $f_{span}$  are the center and spanning frequencies, set on the SG.

Just before the second rising edge of the trigger signal, the SG output is at its highest frequency,

$$f_{high} = f_{center} + f_{span}/2$$

The period of the sweep and corresponding trigger signal was set on the SG.

In order to convert from time to frequency in the oscilloscope data, the data outside of one period of the trigger signal was dropped and the time axis was rescaled such that the first data point corresponded to  $f_{low}$  and the last point corresponded to  $f_{high}$ , with a linear sweep in frequency between.

For example, the data shown in Fig. 18 was rescaled for  $f_{center} = 500kHz$  and  $f_{span} = 340kHz$  and is shown in Fig. 20 below:

In order to find the center of the resonance, the frequencies corresponding to the local minima of the data were identified.

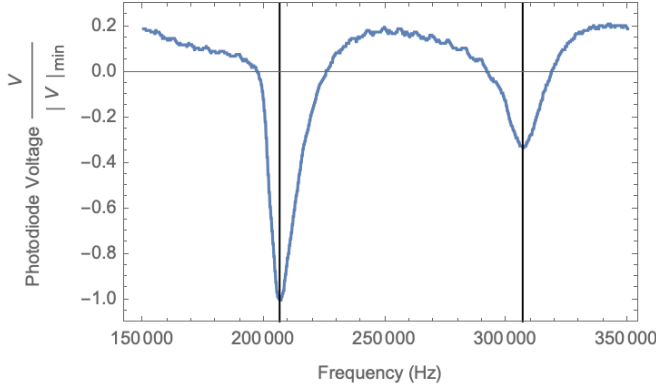


Figure 21. The black lines indicate the measured local minima of dips in transmission corresponding to transitions

In order to estimate the uncertainty on this measurement, a Gaussian of the form

$$fit(x) = A * \exp\left(\frac{-(x - x_0)^2}{\sigma^2}\right) + offset$$

was fit to the data using Mathematica's NonlinearModelFit, with free parameters  $A$  and  $\sigma$ . The parameter  $x_0$  defines the center of the Gaussian, and was taken to be the frequency of the local minimum.

The uncertainty of the measured resonance was taken to be  $\sigma/20$ . An example of the fit to the first dip shown in Fig. 20 is shown in the figure below:

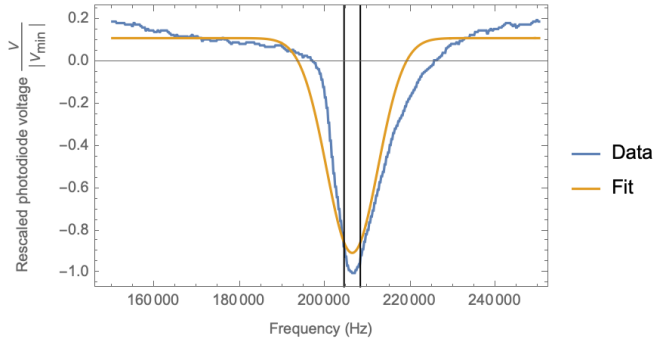


Figure 22. An example of the Gaussian fitting used to estimate the uncertainty of the transition frequency measurement. The data being analyzed is the first peak shown in Fig. 21.

In calculating the uncertainty on a fitted parameter, the parameter was adjusted until the  $\chi^2$  value of the fit increased by 1. The amount that the parameter was adjusted was taken to be the uncertainty.

## IV. MEASUREMENTS

### A. Rubidium lamp warmup time

When taking measurements, we wanted to ensure that output of the lamp was constant over time. It was found that, after turning on the lamp, it took 400s before the lamp output stabilized.

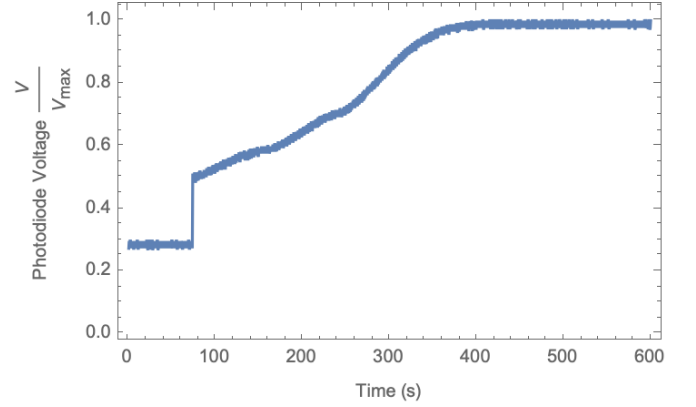


Figure 23. Measured photodiode voltage over time after the lamp was turned on at  $t = 80$ s.

### B. Measurement of absorptive cross section for Rb

By heating the cell and measuring the photodiode voltage as a function of cell temperature, the relationship between transmitted intensity and cell temperature was measured.

In order to measure the relationship between, transmitted intensity and cell temperature, the lamp was first turned on and warmed up. Then, the heat gun was turned on. Simultaneous measurements of photodiode voltage and cell temperature were made. As the temperature measurements were made using a stopwatch, the uncertainty in time was taken to be 0.25s, the human reaction time.

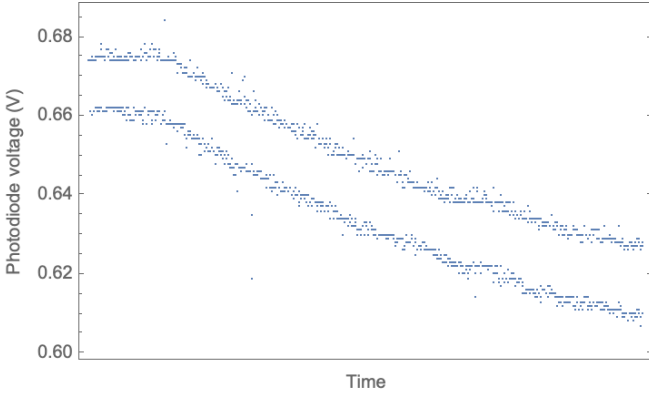


Figure 24. Photodiode signal as a function of time after the heat gun was turned on, slowly heating the Rb cell from  $23^{\circ}\text{C}$  to  $42^{\circ}\text{C}$

As seen in Fig. 24, there was some unfavorable behavior observed in the photodiode voltage signal. It appeared to be splitting into two signals, each with a visually estimated uncertainty of  $\pm 0.0025\text{V}$ . As the general trend of the photodiode voltage and not the exact voltage was of interest, the photodiode signal was averaged, and the uncertainty was taken to be  $\pm 0.0025\text{V}$ .

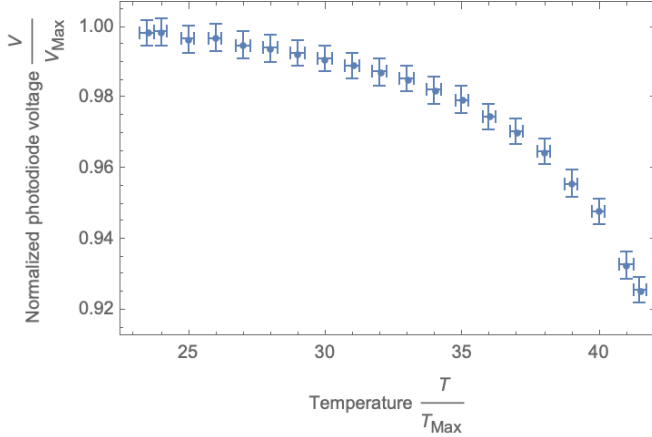


Figure 25. Graph of normalized photodiode voltage vs Rb cell temperature, showing the relationship between vapor temperature and the transmission of light through the cell. This data was used to calculate the absorptive cross section of the Rb vapor in the cell.

In order to find the absorptive cross section  $\sigma$  from the data shown in Fig. 25, the linear relationship between  $\log I(T)$  and  $\sigma$  needed to be found, as discussed in Sec. II F. This required the calculation of  $n(T)$  for each temperature corresponding to a data point in Fig 25.

In this experiment, the absorptive medium was composed of Rb vapor in the solid phase. When the Rb cell is heated to temperature  $T$  the density of atoms in the gas phase can be found by the ideal gas law

$$n(T) = \frac{P_v(T)}{k_B T} \quad (12)$$

where  $P_v(T)$  is the vapor pressure of Rb in the solid phase as a function of temperature and  $k_B$  is the Boltzmann constant.

The vapor pressure of Rb in the solid phase can be approximated by [25]

$$P_v = 10^{2.881 + 4.857 - \frac{4215}{T}} * 133.3224 \quad (13)$$

where  $P_v$  is vapor pressure in Pa, and  $T$  is temperature in Kelvin.

Thus,  $n(T)$  was calculated for each data point.

The plot of  $\log I(T)$  vs  $n(T)z_{\text{cell}}$  is in Fig. 26, together with a linear fit. The uncertainty in  $\log I$  was taken to be

$$\begin{aligned} \frac{\delta \log I}{\log I} &= \frac{\log(I + \delta I) - \log I}{\log I} \\ &= \frac{\log I \log\left(1 + \frac{\delta I}{I}\right) - \log I}{\log I} \\ &= \frac{\log\left(1 + \frac{\delta I}{I}\right)}{\log I} \\ &\approx \frac{\delta I/I}{\log I} \end{aligned}$$

by expanding around the small variable  $\delta I/I$  to lowest order.

The uncertainty in  $n(T)$  was taken to be

$$\frac{\delta n(T)}{n(T)} = \sqrt{\left(\frac{\delta P_v}{P_v}\right)^2 + \left(\frac{\delta T}{T}\right)^2}$$

where

$$\delta P_v(T) = P_v(T + \delta T) - P_v(T)$$

was numerically calculated for each data point.

This uncertainty was added in quadrature with  $\delta z_{\text{cell}}/z_{\text{cell}}$ , where  $z_{\text{cell}} = 5.0 \pm 0.1\text{cm}$  in the experimental setup.

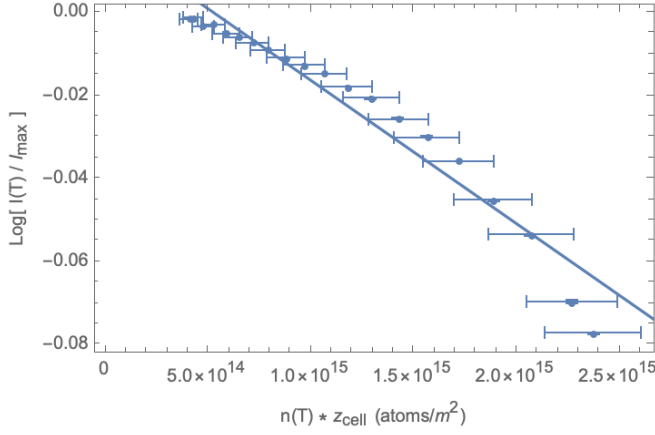


Figure 26. Graph of the logarithm of the transmission vs the calculated density multiplied by cell length, used to calculate the absorptive cross section of Rb in the cell through Beer's law (Eq. 6)

The absorptive cross section, calculated as the absolute value of the slope of the fit shown in Fig. 26, was found to be

$$\sigma = (2.45 \pm 0.02) * 10^{-17} m^2$$

Compared to the theoretical value of  $2.9 * 10^{-13} m^2$  using Eq. 10, this calculated value was off by a factor of  $10^4$ .

When initially taking the measurement, it was noticed that the graph of intensity vs temperature was different depending on if measurements were taken when the temperature was increasing or decreasing. This indicates that the thermometer is not a good indication of the true temperature of the cell, and that this method for calculating absorption cross section cannot be trusted.

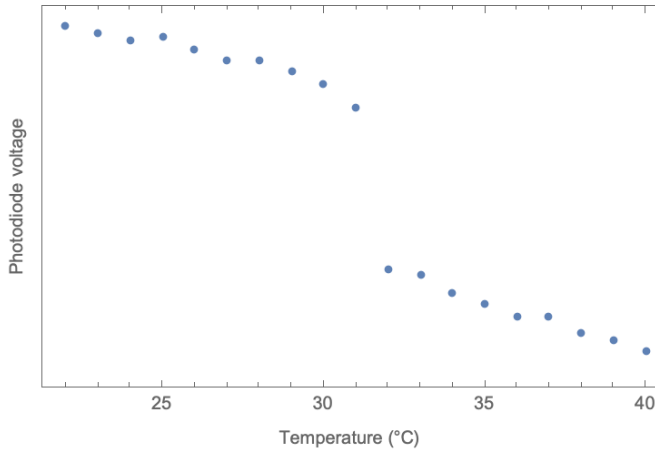


Figure 27. Plot showing the discrepancy in the relationship between transmission and Rb cell temperature. The first 10 data points were taken as temperature was increasing in the Rb cell from  $22^\circ C$  to  $31^\circ C$ , and the last 9 data points were taken as Rb cell was decreasing in temperature from a maximum of  $40^\circ C$  to  $32^\circ C$ .

### C. Power broadening

In order to determine the optimal signal amplitude for the SG producing the RF magnetic field at low external magnetic field, the transmission spectrum was measured for various SG amplitudes, from the minimum of  $10mV$ .

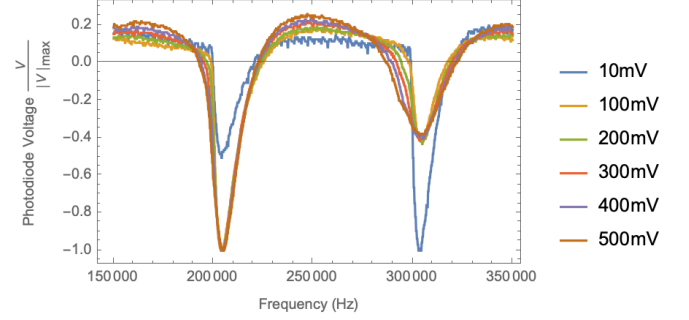


Figure 28. This graph demonstrates the power broadening associated with our sample at a variety of frequencies and voltages.

Notably, for  $10mV$ , the first dip, corresponding to Rb85, is smaller in magnitude than the second dip corresponding to Rb87. For all of the larger signal amplitudes, Rb85 has a larger dip.

Additionally, above an amplitude of  $600mV$ , the amplifier connected to the SG began triggering its overdrive, ruining the spectrum, as seen in Fig 29 below:

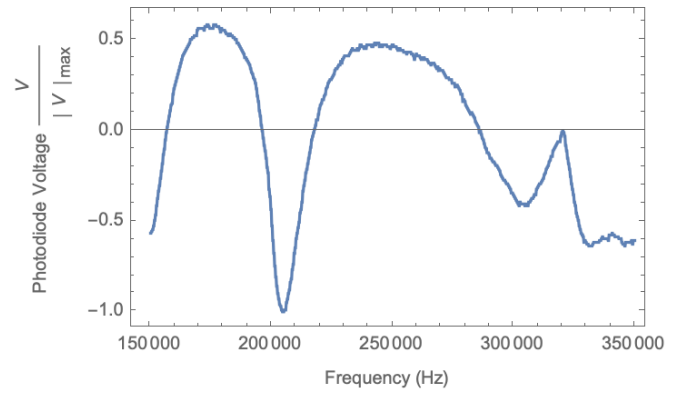


Figure 29. Resonance spectrum in the presence of amplifier overdrive at a SG amplitude of  $600mV$ , showing that the SG amplitude should not be set to more than  $600mV$  when taking the low field measurements

An amplitude of  $250mV$  was chosen for the SG in the experiment described in the following section as it is in the middle of the range of available amplitudes.



### D. Zeeman splitting for small magnetic field

At low magnetic field, where transitions between adjacent  $M_F$  sublevels are approximately equal and thus are not resolvable, the transition frequencies as a function of magnetic field are

$$\nu = \frac{\mu_B g_F B_z}{h} \quad (14)$$

Measurements of the frequency corresponding to the Rb85 and Rb87 transitions are shown in Fig. 30:

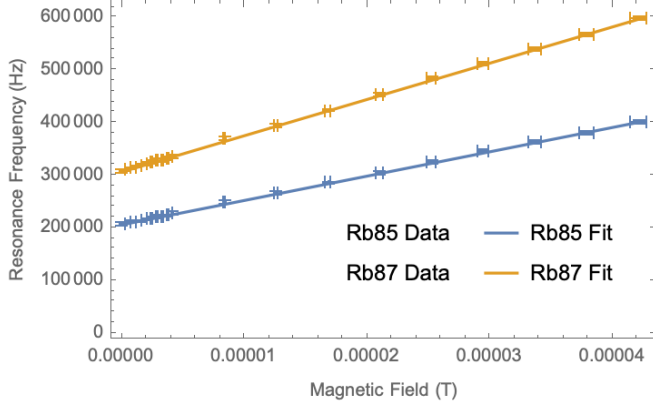


Figure 30. This graph shows the position of the measured resonance for Rb85 and Rb87 vs external magnetic field

As seen in Eq. 14, the slope of the graphs is  $\mu_B g_F B_z / h$ . Thus, using the accepted values of  $\mu_B$  and  $h$  together with a calculated estimate for the field generated by the Maxwell coils,  $B_z$ , the  $g_F$  for Rb85 and Rb87 was calculated.

	Rb85	Rb87
Slope	$4.63 \pm 0.05 \text{ GHz/T}$	$6.91 \pm 0.04 \text{ GHz/T}$

Table III. Fitted slope for transition frequency vs external magnetic field at low magnetic field

Isotope	Theoretical $g_F$	Measured $g_F$
Rb85	0.333	$0.331 \pm 0.004$
Rb87	0.499	$0.493 \pm 0.003$

Table IV. Values of  $g_F$  calculated from the slopes in Tab. III compared to theoretical values found in [25] and [?]

The x-intercept of the linear fit is the offset in magnetic field due to the earth's magnetic field.

Isotope	Calculated earth magnetic field
Rb85	$44.5 \pm 0.3 \mu\text{T}$
Rb87	$44.4 \pm 0.5 \mu\text{T}$

Table V. Measured values of the earth's magnetic field, calculated from the x-intercept of the fitted lines in Fig. 30

In future experiments, the magnetic field should be reversed until the splitting is minimized, and the minimum field can be measured so that this calculation can be verified.

### E. Testing the Breit-Rabi formula

At sufficiently external high magnetic fields the Zeeman shift is no longer approximately linear in  $M_F$ , and thus the various transitions between adjacent  $M_F$  levels become resolvable.

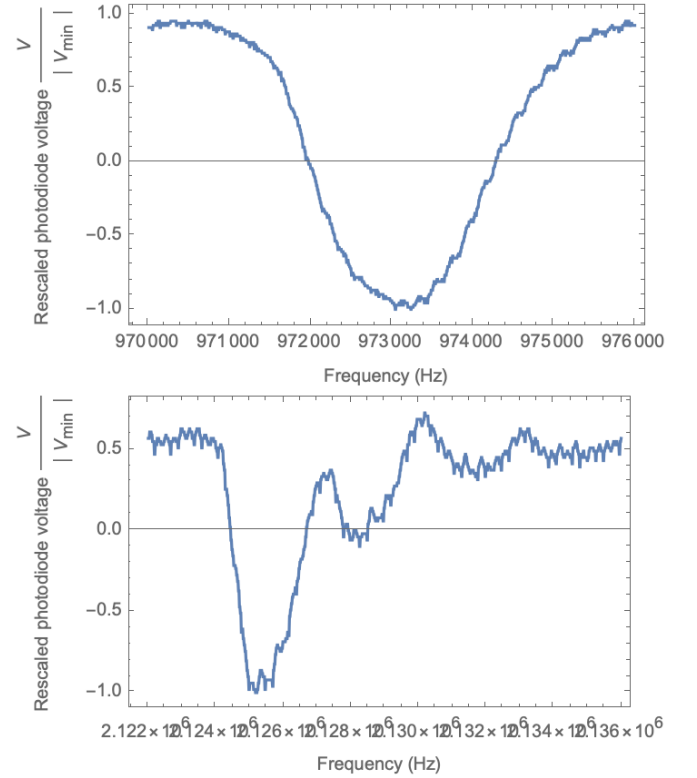


Figure 31. At  $160 \mu\text{T}$  (top), the different transitions between  $M_F$  sublevels could not be resolved. As the magnetic field increased to  $420 \mu\text{T}$  (bottom), the different transitions began to be resolvable.

These energy differences were measured as a function of magnetic field. A plot of the theoretically calculated energy differences vs the measured energy differences is shown in Fig. 32, with the offset due to earth's magnetic field accounted for.



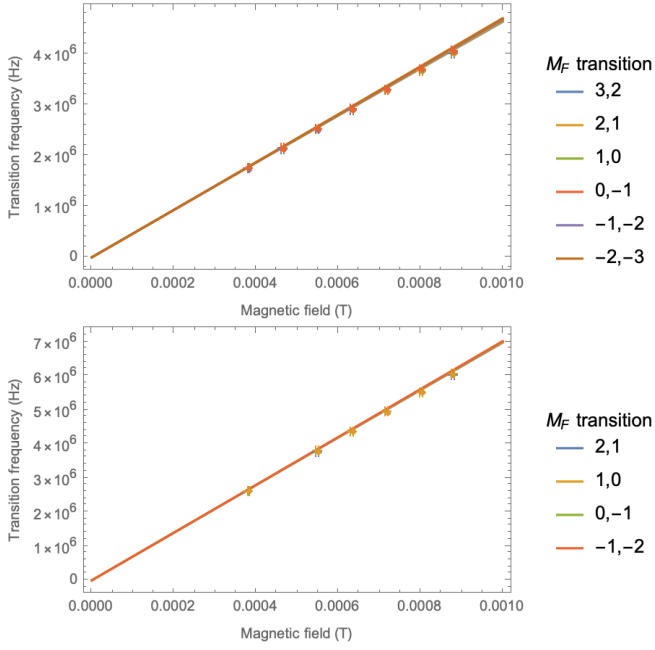


Figure 32. Comparison between data and theory for transition energy for transitions between adjacent  $M_F$  sublevels vs magnetic field for Rb85 (top) and Rb87 (bottom).

Because the transitions were very close in energy, the difference between adjacent transition energies was taken as a function of magnetic field. The comparison between data and theory is shown in Fig. 33 below:

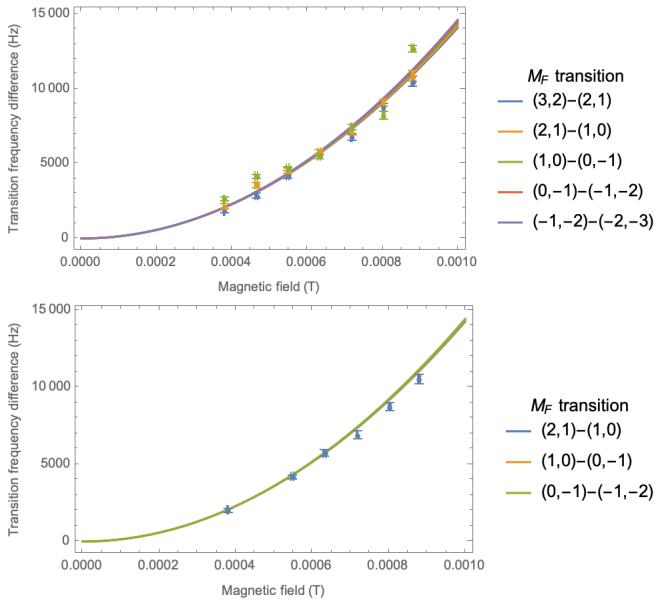


Figure 33. Measured differences between transition energies compared to theoretical values calculated using the Breit-Rabi formula for Rb85 (top) and Rb87 (bottom)

Fig. 34 shows how the different transitions first became resolvable at about  $0.03G$ , and the spacing between

transitions increased at an increasing rate as the external magnetic field increased.

## F. Multi-photon transitions

At the greatest external magnetic field possible in the setup, the greatest possible amplitude on the SG without overdriving the amplifier, and a sweep time of *1second* on the SG, secondary dips were visible in the transmission spectrum, forming directly in between the expected transition frequencies.

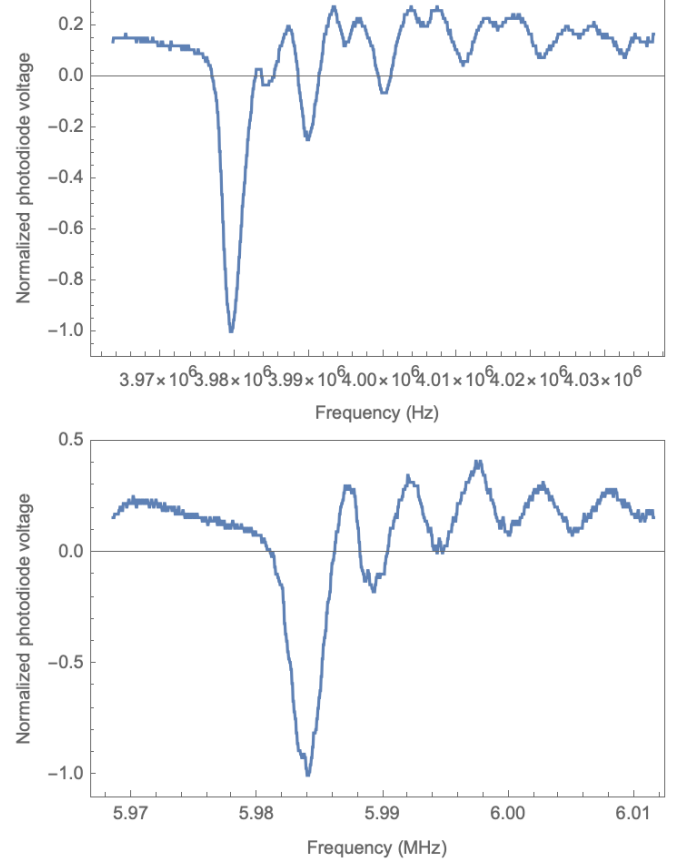


Figure 35. Plots of measured multiphoton transitions in Rb85 (top) and Rb87 (bottom) at an external field of about  $83mT$

At sweep times equal to and below  $500ms$ , these dips did not appear.

## V. CONCLUSION

### A. Measurements

The absorption cross section of Rb was calculated from measured data to be  $\sigma = (2.45 \pm 0.02) * 10^{-17}m^2$ , 4 orders of magnitude smaller than the theoretically calculated value of  $2.9 * 10^{-13}m^2$ . This discrepancy requires

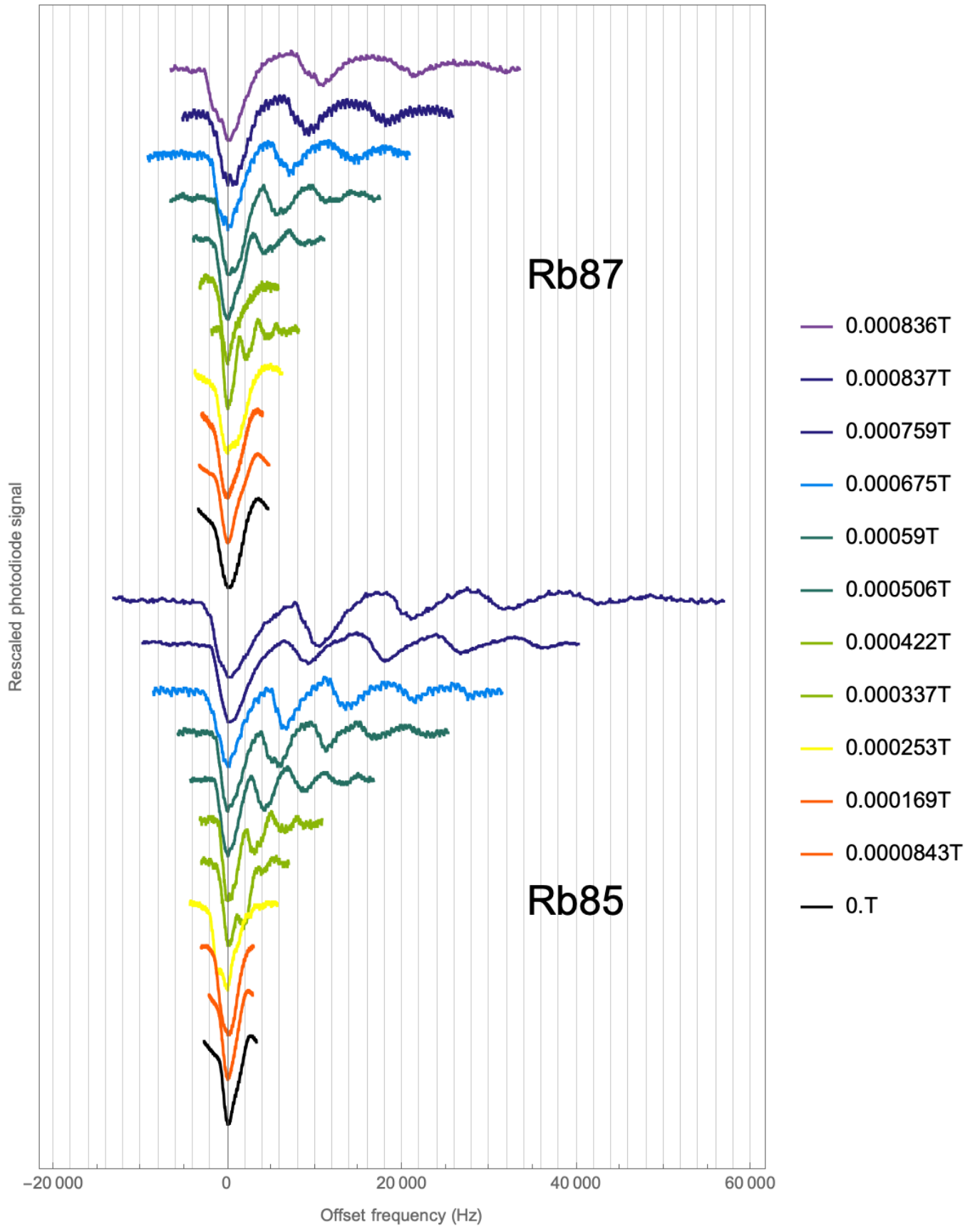


Figure 34. Plot giving a comparison of the differences between transition frequencies as a function of added external magnetic field

further investigation. In order to improve this measurement, the temperature should be fixed when taking the measurement.

In the measurement of power broadening at low magnetic field, it was observed that, for low RF field amplitude, the dip in transmission corresponding to  $^{85}\text{Rb}$  was less extreme than that of  $^{87}\text{Rb}$ , but at high amplitude, this relationship was reversed. It is unclear what causes this behavior.

The measurement of power broadening must be repeated over a range of magnetic fields. There was no clear indication that increased RF field amplitude broadened any features substantially.

Another contributor to the lineshape that should be further investigated is the response time of the Rb vapor to abrupt changes in RF frequency. This effect alters the lineshape at different sweep times. Most of the experiments in this report were done with a sweep time of  $500\text{ms}$ . Only for the multiphoton transition measurements was the sweep time increased to  $1\text{s}$ , as the transitions did not appear at  $500\text{ms}$ .

The calculated earth magnetic field of  $44.4 \pm 0.05\mu\text{T}$  was on the same order of magnitude as the expected value of  $\approx 51.22\mu\text{T}$  [? ], with a percent error of around  $\approx 13.05\%$ . The discrepancy is likely due to misalignment of the apparatus with the earth's magnetic field. Thus, it

is estimated that the lowest possible field that can be generated with the apparatus is  $(51.22 - 44.4)\mu\text{T} \approx 7\mu\text{T}$ . In future experiment, the magnetic field from the Maxwell Coils should be used to cancel out the earth's field as much as possible in order to measure the minimum possible magnetic field.

The measured  $g_F$  for Rb85 was  $0.331 \pm 0.004$ , consistent with the theoretical value of  $0.333$ . For Rb87, a  $g_F$  of  $0.493 \pm 0.003$  was measured, inconsistent with the theoretical value but within  $2\%$ .

At intermediate fields, the Breit-Rabi formula was verified. Multi-photon transitions were also successfully observed.

## B. Suggested improvements

One of the largest sources of systematic error in this experiment was the measurement of the photodiode on AC coupling mode. At long sweep times, AC coupling might have significantly distorted the signal. In a future setup, we will set the photodiode to DC coupling and used a power supply to subtract any DC offset to the signal. Additionally, a larger capacitor will be used to filter out  $60\text{Hz}$  noise affecting the photodiode signal. Improving the signal-to-noise is vital to improving the setup.

- 
- [1] J. J. Thomson, XI. cathode rays, The London, Edinburgh, and Dublin Philosophical Magazine and Journal of Science **44**, 293 (1897).
  - [2] P. Zeeman, Nobel lecture: Light radiation in a magnetic field (1903).
  - [3] H. Schmidt-Böcking, G. Gruber, and B. Friedrich, One hundred years ago alfred landé unriddled the anomalous zeeman effect and presaged electron spin, Physica Scripta **98**, 014005 (2022).
  - [4] G. E. Uhlenbeck and S. Goudsmit, Ersetzung der hypothese vom unmechanischen zwang durch eine forderung bezüglich des inneren verhaltens jedes einzelnen elektrons, Die Naturwissenschaften **13**, 953 (1925).
  - [5] E. D. Commins, Electron spin and its history, Annual Review of Nuclear and Particle Science **62**, 133 (2012), <https://doi.org/10.1146/annurev-nucl-102711-094908>.
  - [6] B. Friedrich, G. Meijer, H. Schmidt-Böcking, and G. Gruber, One hundred years of alfred landé's g-factor, Natural Sciences **1**, e20210068 (2021).
  - [7] A. Landé, Über den anomalen zeemaneffekt (teil i), Zeitschrift für Physik **5**, 231 (1921).
  - [8] A. Kastler, Nobel lecture 1966, Phys. Today **20**, 34 (1967).
  - [9] A. Kastler, Optical methods for studying hertzian resonances, Science **158**, 214 (1967).
  - [10] A. Sommerfeld, *Atomabau und Spektrallinien* (1924).
  - [11] C. V. Raman and S. Bhagavantam, Experimental proof of the spin of the photon, (1931).
  - [12] S. N. Bose, Planck's law and the light quantum hypothesis, Journal of Astrophysics and Astronomy **15**, 3 (1994).
  - [13] A. Kastler, *Recherches sur la fluorescence visible de la vapeur de mercure*, Ph.D. thesis, Université de Paris (1936).
  - [14] F. Bitter, The optical detection of radiofrequency resonance, Physical Review **76**, 833 (1949).
  - [15] J. B. M. Kellogg and S. Millman, The molecular beam magnetic resonance method. the radiofrequency spectra of atoms and molecules, Rev. Mod. Phys. **18**, 323 (1946).
  - [16] W. E. Lamb Jr, Fine structure of the hydrogen atom, Science **123**, 439 (1956).
  - [17] A. Kastler, Quelques suggestions concernant la production optique et la détection optique d'une inégalité de population des niveaux de quantification spatiale des atomes. application à l'expérience de stern et gerlach et à la résonance magnétique, J. phys. radium **11**, 255 (1950).
  - [18] T. H. Maiman, Stimulated optical radiation in ruby, Nature **187**, 493 (1960).
  - [19] C. N. Cohen-Tannoudji, Nobel lecture: Manipulating atoms with photons, Reviews of Modern Physics **70**, 707 (1998).
  - [20] I. Žutić, J. Fabian, and S. D. Sarma, Spintronics: Fundamentals and applications, Reviews of modern physics **76**, 323 (2004).
  - [21] P. van der Straten and H. Metcalf, Fine structure, in *Atoms and Molecules Interacting with Light: Atomic Physics for the Laser Era* (Cambridge University Press, 2016).
  - [22] D. J. Griffiths and D. F. Schroeter, *Introduction to Quantum Mechanics*, 3rd ed. (Cambridge University Press, 2018).

- [23] T. Allison, *PHY 445/515 Optical Pumping and Magnetic Resonance*, Stony Brook University (2015).
- [24] J. Sakurai, *Advanced Quantum Mechanics*, Always learning (Pearson Education, Incorporated, 2006).
- [25] D. A. Steck, *Rubidium 85 D Line Data*, University of Oregon (2021).
- [26] D. A. Steck, *Rubidium 87 D Line Data*, University of Oregon (2021).
- [27] Absorption, emission, and dispersion of light, in *Laser Physics* (John Wiley Sons, Ltd, 2010) Chap. 3, pp. 67–140.